

PYROCLASTICS NORTHEAST OF GASSENDI CRATER: DISCOVERY/CHARACTERISTICS/IMPLICATIONS. T.A. Giguere¹, B.R. Hawke¹, D. Trang¹, L.R. Gaddis², S.J. Lawrence³, J.D. Stopar⁴, J.O. Gustafson⁵, J.M. Boyce¹, J.J. Gillis-Davis¹, and the LROC Science Team⁶. ¹Hawaii Institute of Geophysics and Planetology, Univ. of Hawaii, Honolulu, HI 96822, ²U.S. Geological Survey, Astrogeology Science Center, Flagstaff, AZ 86001, ³Johnson Space Center, Houston, TX, ⁴Lunar and Planetary Institute, Houston, TX, ⁵Cornell Univ., Ithaca, NY 14850, ⁶School of Earth and Space Exploration, Arizona State Univ., Tempe, AZ 85281 (giguere@hawaii.edu).

Introduction: We are investigating pyroclastic deposits in the Gassendi region to better understand aspects of lunar volcanism. Interest in lunar pyroclastic deposits (LPDs) has remained high due to the availability of high spatial-resolution data (i.e., LRO, Kaguya), used to build on previous remote sensing studies [e.g., 1, 2, 3] and those focused on lunar pyroclastic glasses [4, 5]. Analyses conducted in the laboratory of pyroclastic spheres from several deposits show that some volcanic glasses had a greater depth of origin and lesser fractional crystallization than mare basalts [e.g., 4, 6]. Pyroclastic glasses likely are the best examples of primitive materials on the Moon, and they are important for both characterizing the lunar interior and as a starting place for understanding the origin and evolution of lunar basaltic magmatism [2].

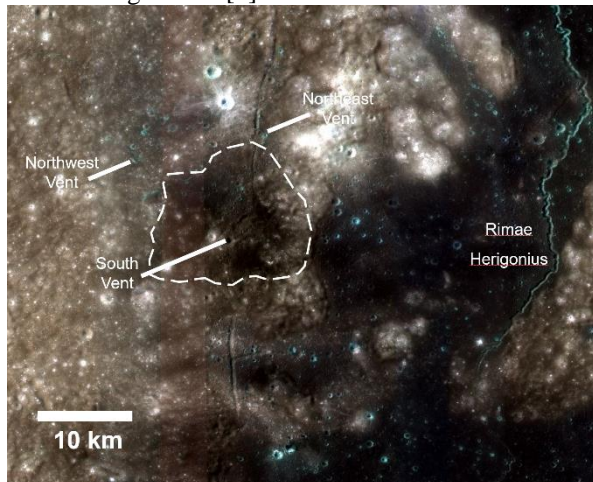


Figure 1. Northeast pyroclastics and three vents (arrowed). The white-dashed outlines the primary deposit. Data from the Kaguya Multiband Imager, with a spatial resolution of ~ 20 m/pixel [18]; false-color view (red=band 3, 900 nm; green=band 2, 700 nm; blue=band 1, 415 nm). North is up.

We analyzed Lunar Reconnaissance Orbiter Camera (LROC) Wide Angle Camera (WAC) and Narrow Angle Camera (NAC) images, and Kaguya Multiband Imager (MI) and Terrain Camera (TC) images, and other spacecraft data to examine the Gassendi region to search for previously unidentified pyroclastic deposits [e.g., 3]. Multiple pyroclastic deposits and associated vents were identified to the northeast of Gassendi crater. These deposits are examined with the methods established by recent work based on the latest spacecraft data [3, 7, 8]. The purposes of this study are as follows: (1) To identify and characterize previously unknown localized pyroclastic deposits, (2) To determine the composition of the

pyroclastic units, (3) To measure deposit block populations, thicknesses and in turn the volume, (4) To investigate the eruption characteristics.

Data and Methods: Both WAC (high and low incidence) and NAC images were used in this study [9, 10]. Topographic data were provided by the LROC GLD100 [11] digital topographic model (DTM). The LRO Diviner Lunar Radiometer Experiment surface rock abundance map data at 128 m/pixel [12, 13] were used to characterize the abundance of blocks >1 m in size on and near the deposits.

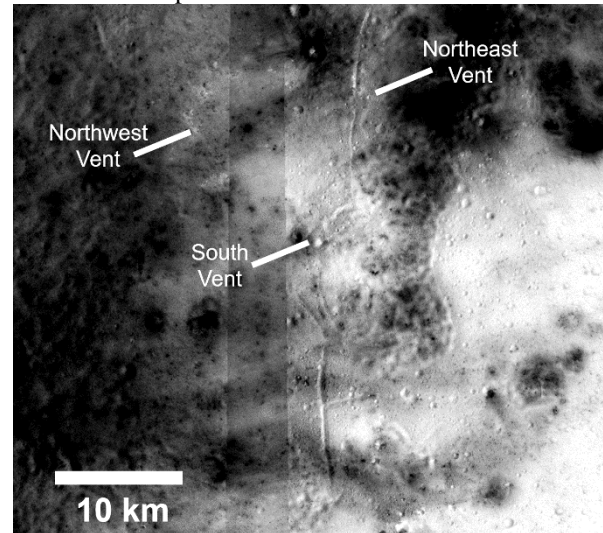


Figure 2. Northeast pyroclastics and three vents (arrowed). Kaguya MI FeO image. North is up.

The Clementine 5-color UV-VIS digital image model (DIM; [14]) were used to produce OMAT, FeO and TiO₂ maps [15, 16] and for 5-point spectra.

Image data from the SELENE “Kaguya” monochromatic TC [17] and the MI [18] visible and near-infrared multispectral camera were used for detailed surface and geochemical analysis. The thickness and volume of the localized pyroclastic deposit was calculated from the Wide Angle Camera (WAC) and Kaguya digital terrain models (DTM) using methods similar to [19].

Results and Discussion: The pyroclastic deposit (Figure 1) is located ~ 45 km to the northeast of the NW Gassendi crater rim at $15.0^{\circ}\text{S } 37.7^{\circ}\text{W}$ and it subtends an area of $\sim 20 \times 20$ km². The geologic map of Marshall [20] shows the terrain is largely Imbrium-aged material (Ir) with possible “Procellarian”-aged (now Upper Imbrian) mare at the south end of the pyroclastic. A lineament is mapped through the deposit, and is interpreted as a fault

or fracture. Our results find that the previously mapped mare unit, while low in albedo, is a dark-mantling, pyroclastic deposit which blankets hills and depressions in the area. Pyroclastic material is observed on the hills east of the main deposit, which is 1000 meters higher in elevation. NAC data provides a detailed view of the lineament which is roughly parallel to Rima Herigonius to the east; the lineament is less sinuous than the Herigonius rille thus is more likely to be a structural feature.

Three vents have been located, two are north of the main deposit (Northwest vent, Northeast vent), while the South vent is in the mapped pyroclastic deposit (Figures 1-4). The vents were identified based on morphology, low albedo, and geochemical signature. The Northwest vent (14.8°S, 38.1°W) is 800 x 500 m and is line with a northwest-southeast trending rille. The Northeast vent (14.7°S, 37.7°W) is in line with the north-south rille, is roughly circular (1.4 x 1.4 km) and has an adjoining linear vent section to the north. The South vent is the largest of the three, roughly rectangular in shape, and is 3 x 2 km² in size. At 120 m the South vent is the deepest of the three vents (Figure 3).

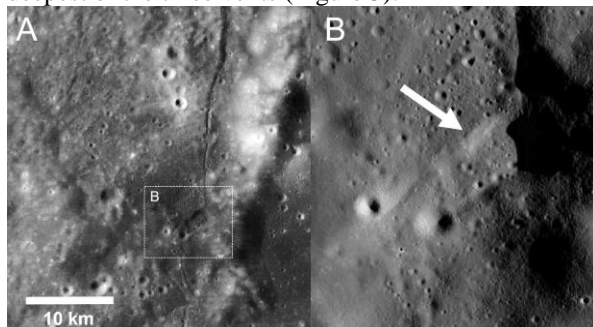


Figure 3. A) South vent area (Clementine 750 nm), B) NAC image of the south vent (NAC M193203275L&R). North is up.

The Kaguya [18] and Clementine [15, 16] geochemical datasets were examined to understand the composition of the pyroclastics deposits. The entire area shows elevated FeO value (i.e. >12 wt%) and the defined pyroclastic region (white dashed area in Figure 1) exhibits FeO values averaging 14-16, with the highest values approaching 17 wt% (Figure 2). The elevated values continue to the north of the other two vents, however, is interrupted by a secondary crater chain which disrupts the regolith and lowers the Fe values. The distribution of TiO₂ matches the distribution of the Fe-rich material. The highest TiO₂ values range between 3 and 4 wt%.

A sample area to the northwest of the South vent was selected to determine the rock abundance in the pyroclastic deposit excluding two fresh craters within the deposit. The mean surface rock abundance for this deposit is 0.30% with a std. deviation of 0.10%. This surface rock abundance value is within the range of the surface rock abundance of the Alphonsus localized pyroclastic deposits, which have a mean value of 0.32% [8]. These values may be compared to the modal rock abundances

for regional pyroclastic deposits, highlands, and maria are 0.3, 0.4, and 0.5%, respectively [13].

Color ratio images (Figure 4) cancel out the dominant brightness variations in multispectral scenes caused by albedo variations and topographic shading and isolate the color variations related to mineralogy or maturity (e.g. 21, 22). Immature highlands presents as aqua, iron-rich volcanic materials are yellowish, and both impact melts [22] and glassy Fe²⁺-rich pyroclastics [21] appears as deep red. The South vent area has no large, fresh impacts nearby, thus impact melt is not present; glass rich pyroclastics blanket and surround the South vent. Additional confirmation is planned using Kaguya mineral mapping techniques [23].

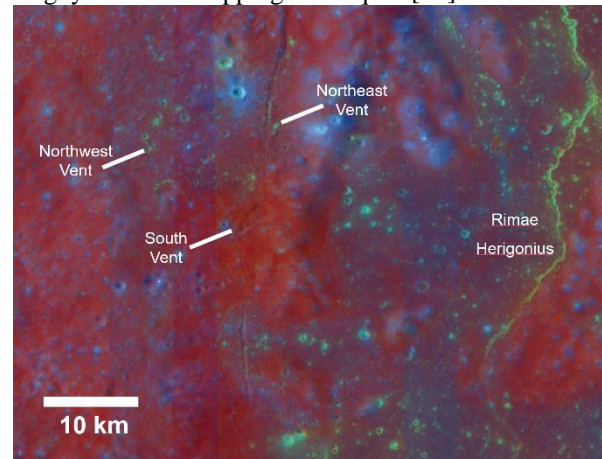


Figure 4. Northeast pyroclastics and three vents (arrowed). Kaguya MI color-ratio (red=750/415, green=750/950, blue=415/750 nm).

Summary: Observations suggest the presence of a glass rich pyroclastic deposit to the NW of Gassendi crater. A primary vent (South vent) was identified based on morphology, physical properties, low albedo, and geochemical data. Smaller vents were identified to the northwest and northeast, and may have contributed a lesser amount of pyroclastic material to the overall deposit.

References: [1] Gaddis L. et al. (1985) *Icarus*, 61, 461. [2] Gaddis, L. et al. (2003) *Icarus*, 161, 262-280. [3] Gustafson, O. et al. (2012) *JGR*, 117, E00H25. [4] Shearer C. and Papike J. (1993) *GCA*, 57, 4785. [5] Hagerty J. et al. (2006) *GCA*, 70, 3457. [6] Papike J. et al. (1998) *Rev. Miner.*, 36, 5.1. [7] Gaddis, L. et al. (2016) *LPSC XLVII*, #2065. [8] Trang, D et al. (2017) *Icarus*, 283, 232-253. [9] Robinson, M. et al. (2010) *Spac Sci. Rev.* 150, 81. [10] Speyerer, E. et al. (2011) *LPSC XLII*, #2387. [11] Scholten F. et al. (2012) *JGR*, 117, 12 pp. [12] Paige et al. (2010), *Spac Sci. Rev.*, 150, 125-160. [13] Bandfield et al. (2011), *JGR*, 116, E00H02. [14] Eliason E. et al. (1999) *LPS XXX*, #1933. [15] Lucey P. et al. (2000) *JGR*, 105 (E8), 20,297. [16] Lucey P. et al. (2000) *JGR*, 105 (E8), 20,377. [17] Haruyama et al. (2008) *Earth Plan. Space*, 60, 243– 256. [18] Ohtake, M. et al. (2008) *Earth Plan. Space*, 60, 257-264. [19] Head J. W. and Wilson L. (1979), *Proc. Lunar Sci. Conf. 10th*, 10, 2861–2897. [20] Marshall C. (1963) *U.S.G.S. Map I-385*. [21] Pieters, C.M. et al. (1994) *Science*, 266, 1844. [22] McEwen, A.S. et al. (1994) *Science*, 266, 1858. [23] Lemelin, M. et al. (2015) *JGR*, 120, 869-887.